Journal of Physics and Chemistry of Solids 104 (2017) 145–151

Contents lists available at ScienceDirect

Journal of Physics and Chemistry of Solids

journal homepage: www.elsevier.com/locate/jpcs

Phase stability in the Cu-9 wt%Al-10 wt%Mn-3 wt%Ag alloy

C.M.A. Santos[a], A.T. Adorno[a], A. Paganotti[b], C.C.S. Silva[b], A.B. Oliveira[b], R.A.G. Silva[a,b,*]

[a] IQ, Universidade Estadual Paulista, Campus Araraquara, SP, Brazil
[b] DCET, Universidade Federal de São Paulo, Campus Diadema, SP, Brazil

ARTICLE INFO

Keywords:
Cu-based alloys
Phase stability
Bainitic precipitation

ABSTRACT

The phase stability in the Cu-9 wt%Al-10 wt%Mn-3 wt%Ag alloy was analyzed using differential scanning calorimetry (DSC), X-ray diffractometry (XRD), transmission electron microscopy (TEM), high-resolution transmission electron microscopy (HRTEM), optical microscopy (OM) and microhardness measurements with quenching temperature. The results showed that the presence of silver alters the phase stability range and enhances the effect of bainite precipitation on the microhardness values of the Cu-9 wt%Al-10 wt%Mn-3 wt%Ag alloy.

1. Introduction

Shape memory alloys (SMAs) are widely used in electronic communications, biomedicine, micro-electromechanics systems, aerospace, robotics, civil construction and many other fields [1,2]. Among the various SMAs, Cu-based SMAs are the most potential ones for large-scale industrial applications because of their low cost, high electrical and thermal conductivity [3]. Single-crystal Cu-based SMAs exhibit excellent shape memory properties, which are almost equivalent to those of Ni-Ti SMAs [1,2]. Compared with other Cu-based ternary alloys, Cu-Al-Mn system has some interesting properties due to the presence of manganese.

The Mn makes the β (bcc) phase more stable to diffusional decomposition and retards this reaction, and the β phase becomes metastable. Because of this, more adequate shape-memory properties can be obtained, and Cu-Al-Mn or Cu-Al-Mn-based alloys have been preferred for some technological applications rather than other Cu-based alloys. Cu-Al-Mn alloys have magnetic ordering properties, whose specific features depend on the crystallographic phase and the composition of each alloy. Thus, the Heusler phase Cu_2MnAl is ferromagnetic, with a relatively high Curie temperature (630 K) and Cu_3Mn_2Al is antiferromagnetic [4]. These properties are due to the RKKY interaction among the Mn atoms of the crystalline lattice [5,6]. The magnetic degrees of freedom make Cu-Al-Mn alloys very interesting from a fundamental point of view, since the interaction between magnetic, elastic and configurational properties can be studied in these alloys [4].

The Cu-Al-Mn alloys can present ordered structures with B2-β_2, $D0_3$-β_1 or $L2_1$-β_3 type superlattices. These phases can transform into martensite phase during fast cooling [7]. During quenching from β(A2) phase region, these alloys undergo a sequence of ordering reactions $\beta(A2)\rightarrow\beta_2(B2)\rightarrow\beta_3(L2_1)$. In the composition range above 16 at% Al the $L2_1$ phase martensitically transforms to the 6 M structure, while in the composition range below 16 at% Al the ordering from A2 to $L2_1$ structure is suppressed by quenching and the martensitic transformation from A2 to 2 M (A1, disordered face-centred cubic) occurs at low temperatures. The critical temperature of martensitic transformation can change from ~200 to~373 K depending on Al and Mn concentration [8]. Different atomic elements were added to the Cu-Al-Mn alloys [9–11] to improve some system properties. This work intends to study the effects of Ag addition on the phases stability of the Cu-9 wt%Al-10 wt%Mn-3 wt%Ag alloy quenched from 1123 K in iced water.

2. Experimental procedures

The Cu-9 wt%Al-10 wt%Mn-3 wt%Ag (Cu-18.8 at%Al-10.3 at%Mn-1.6 at%Ag) alloy was prepared in an arc furnace under argon atmosphere using 99.95% copper, 99.97% aluminum, 99.995% manganese and 99.98% silver as starting materials. Cylindrical samples with 2.0 cm diameter and 6.0 cm length were cut in disks with thickness of 2.0 mm. The samples were maintained for 4.32×10^5 s at 1123 K and then cooled at 1.0 $Kmin^{-1}$ down to room temperature for samples homogenization after melting.

In this work two different heat treatments were made after homogenization. Firstly, the alloy was analyzed after kept for 3.6×10^3 s at 1123 K and then quenched in iced water to produce the metastable phases, as shown in Fig. 1. This heat treatment will be called HT_1.

The second heat treatment consisted to keep the samples for

* Corresponding author at: DCET, Universidade Federal de São Paulo, Campus Diadema, SP, Brazil.
E-mail address: galdino.ricardo@gmail.com (R.A.G. Silva).

http://dx.doi.org/10.1016/j.jpcs.2017.01.012
Received 5 October 2016; Received in revised form 16 December 2016; Accepted 12 January 2017
Available online 12 January 2017
0022-3697/

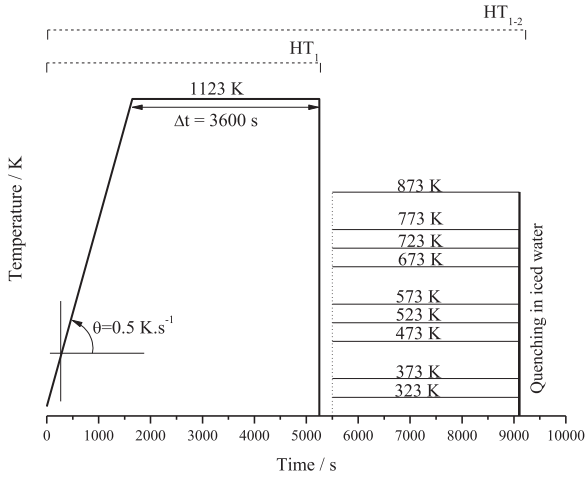

Fig. 1. Scheme of the thermal treatments used in this work.

3.6×10^3 s at 1123 K and then quenched in iced water. In sequence, the samples quenched from 1123 K were inserted in a furnace at a given defined temperature and kept for 3.6×10^3 s in this condition, and then again quenched in iced water as seen in Fig. 1. This heat treatment will be called $HT_{1\rightarrow2}$. The procedure was made to follow the evolution of the metastable phases until the formation of more stable phases in the alloy. These defined temperatures are here called "quenching temperatures". For each quenching temperature was used a different sample of the Cu-9 wt%Al-10 wt%Mn-3 wt%Ag alloy.

The DSC curves were obtained using a DSC Q20 TA Instruments at different heating rates. Transmission electron micrographs and high-resolution transmission electron micrographs were obtained using a Philips microscope, model CM200, operating at 200 keV. Optical microscopy was made from an Olympus microscope BX41M-LED. The Vickers microhardness measurements were made with a HMV-2T SHIMADZU TESTER using a load of 9.8 N. The X-ray diffraction (XRD) patterns were obtained using a Bruker D8 Advanced AXS diffractometer, Cu Kα radiation, solid (not powdered) samples and rotation of 30 rpm. The X-ray diffraction patterns were refined using the Rietveld method [12] and the TOPAS software [13] to quantify the phases in the studied alloy.

3. Results and discussion

The crystal structures of the phases in the Cu-9 wt%Al-10 wt%Mn-3 wt%Ag alloy submitted to HT_1 were examined by transmission electron microscopy (TEM), high-resolution transmission electron microscopy (HRTEM) and selected area diffraction pattern (SADP) techniques. Fig. 2-a, b and c show the TEM bright-field images (BFI) and its selected area diffraction patterns (SADP) taken from a Cu-9 wt%Al-10 wt%Mn-3 wt%Ag specimen submitted to HT_1. The SADP images exhibit spots of electron diffraction patterns from the α-Cu rich phase (Fig. 2-a) and the $\beta_3(L2_1)$ phase (Fig. 2-b). The observed Debye-Scherrer rings (Figs. 2-a and 2-b) are characteristics of Ag nanoprecipitates. The high-resolution image (Fig. 2-c) from one precipitate shows an interlayer spacing of 0.235 nm, which corresponds to the (111) lattice plane spacing for Ag. Fig. 2-d exhibits a TEM bright-field image and a HRTEM image of another phase that shows an interlayer spacing of 0.237 nm, which corresponds to the (202) lattice plane spacing for the $\beta_1(D0_3)$ phase.

In this way, immediately after quenching from 1123 K in iced water (HT_1) the Cu-9 wt%Al-10 wt%Mn-3 wt%Ag alloy presents the α-Cu rich, $\beta_3(L2_1)$ and $\beta_1(D0_3)$ phases together with Ag nanoprecipitates. In Cu-Al-Ag alloys with Ag content around 3 wt%, it is not possible to verify Ag precipitates after quenching from 1123 K in iced water because Ag is dissolved in the matrix and then it only precipitates during reheating [14]. This behavior indicates that the addition of 10 wt%Mn decreases the silver solubility in the Cu-9 wt%Al alloy and

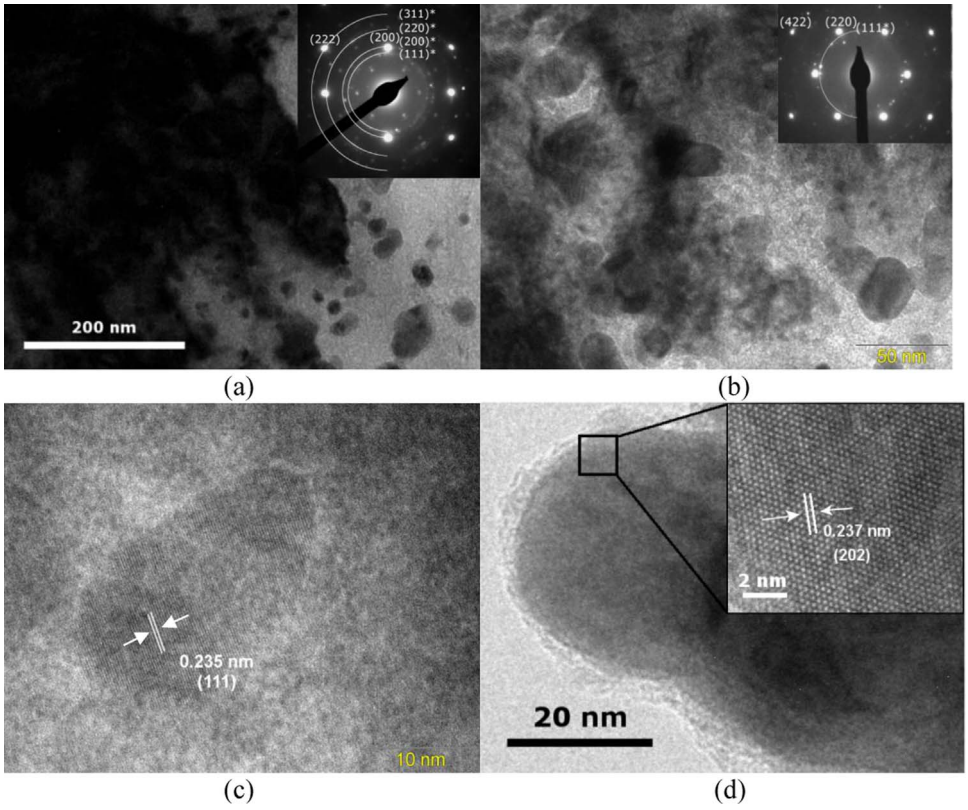

Fig. 2. TEM bright-field images and its selected area diffraction patterns from: (a) α-Cu-rich phase and (b) $\beta_3(L2_1)$ phase. (c) HRTEM image showing details from Ag nanoprecipitate. (d) TEM bright-field image and a HRTEM image from the $\beta_1(D0_3)$ phase.

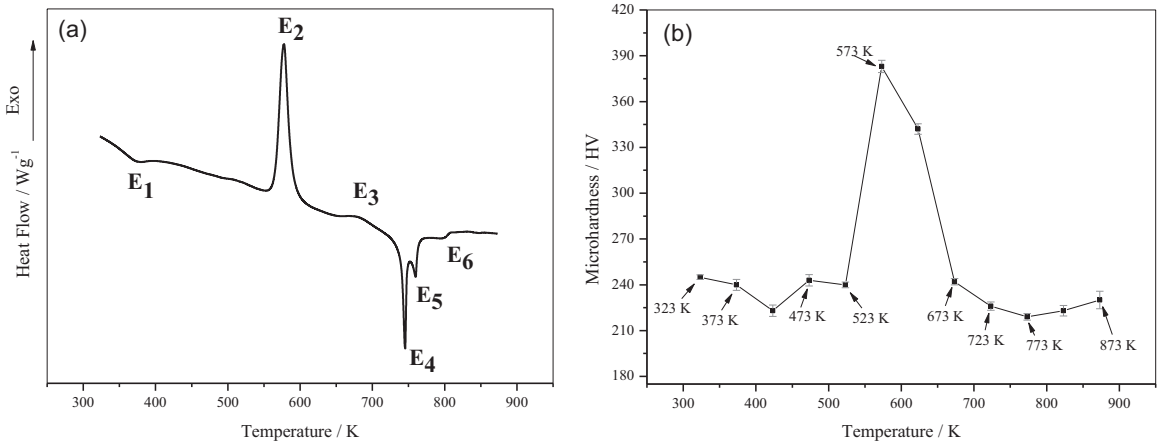

Fig. 3. (a) DSC curve obtained with heating rate of 3 K min^{-1} for a sample initially submitted to HT_1. (b) Microhardness with quenching temperature curve obtained as described in $HT_{1\rightarrow2}$ of Fig. 1.

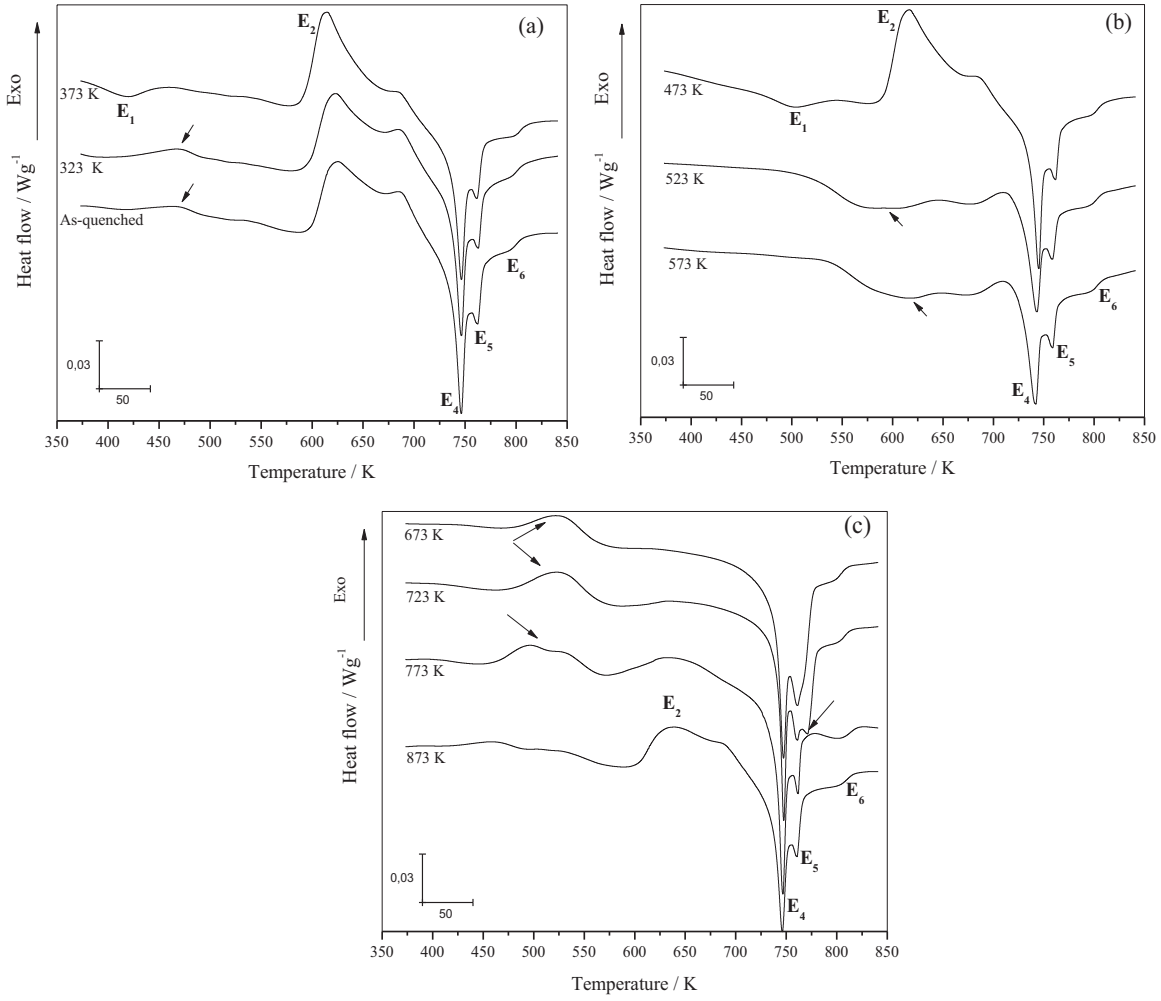

Fig. 4. DSC curves obtained with a heating rate of 10 K min^{-1} for samples of the Cu-9 wt%Al-10 wt%Mn-3 wt%Ag alloy initially submitted to $HT_{1\rightarrow2}$.

induces the formation of Ag nanoprecipitates in samples quenched from 1123 K in iced water.

Fig. 3-a shows the DSC curve obtained with a heating rate of 3 K min^{-1} for a sample of the Cu-9 wt%Al-10 wt%Mn-3 wt%Ag alloy initially submitted to HT_1. This DSC curve shows six thermal events. The endothermic peak E_1 corresponds to the decomposition of the $\beta_3(L2_1)$ phase, peak E_2 at about 570 K is due to the bainitic precipitation and decomposition of the $\beta_1(D0_3)$ phase, producing the T_3-Cu_3AlMn_2, β_{Mn} and α phases. Therefore, in this case, the thermal event E_2 may be associated with other reactions, in addition to bainitic precipitation. Literature data obtained for the Cu-18at%Al-11at%Mn alloy shows only bainitic precipitation in this temperature range [15]. The precipitation of Ag retained in the matrix [16] occurs in sequence and is evidenced by peak E_3 at about 673 K. The thermal event E_4 can be due to the re-dissolution of Ag precipitates [17] and the T_3-Cu_3AlMn_2+α+$\beta_{Mn}\rightarrow\beta_2(B2)$+$T_3$-$Cu_3AlMn_2$+α transformation, while E_5

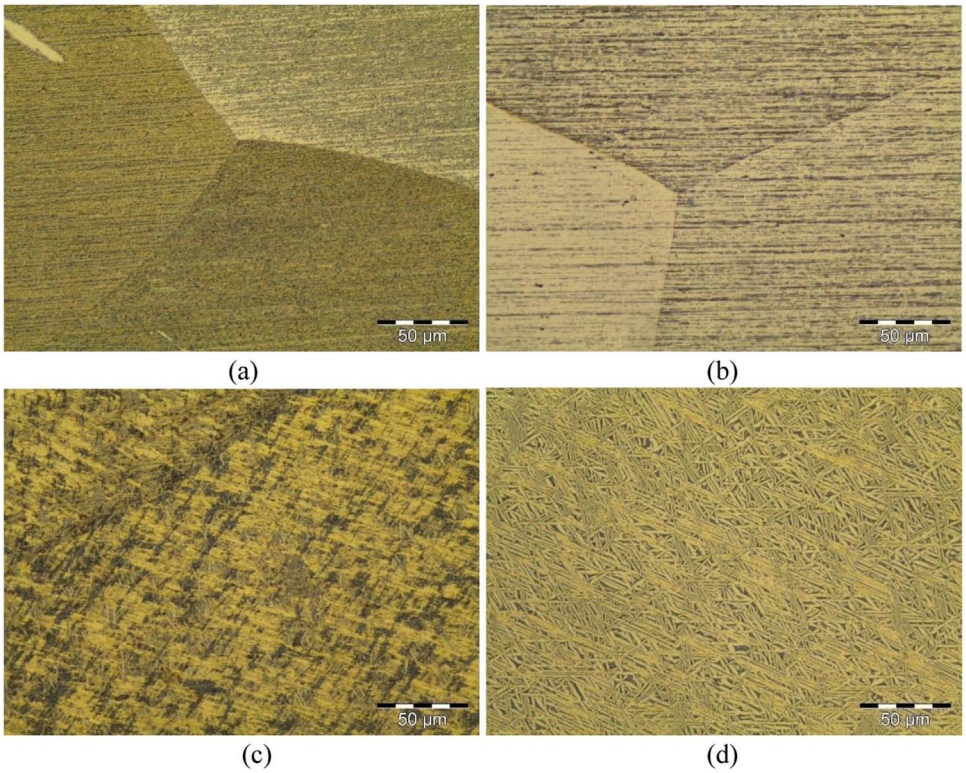

Fig. 5. Optical micrographs (OM) obtained for samples quenched from (a) 1123 K in iced water and then again quenched in iced water from (b) 523 K, (c) 573 K and (d) 673 K.

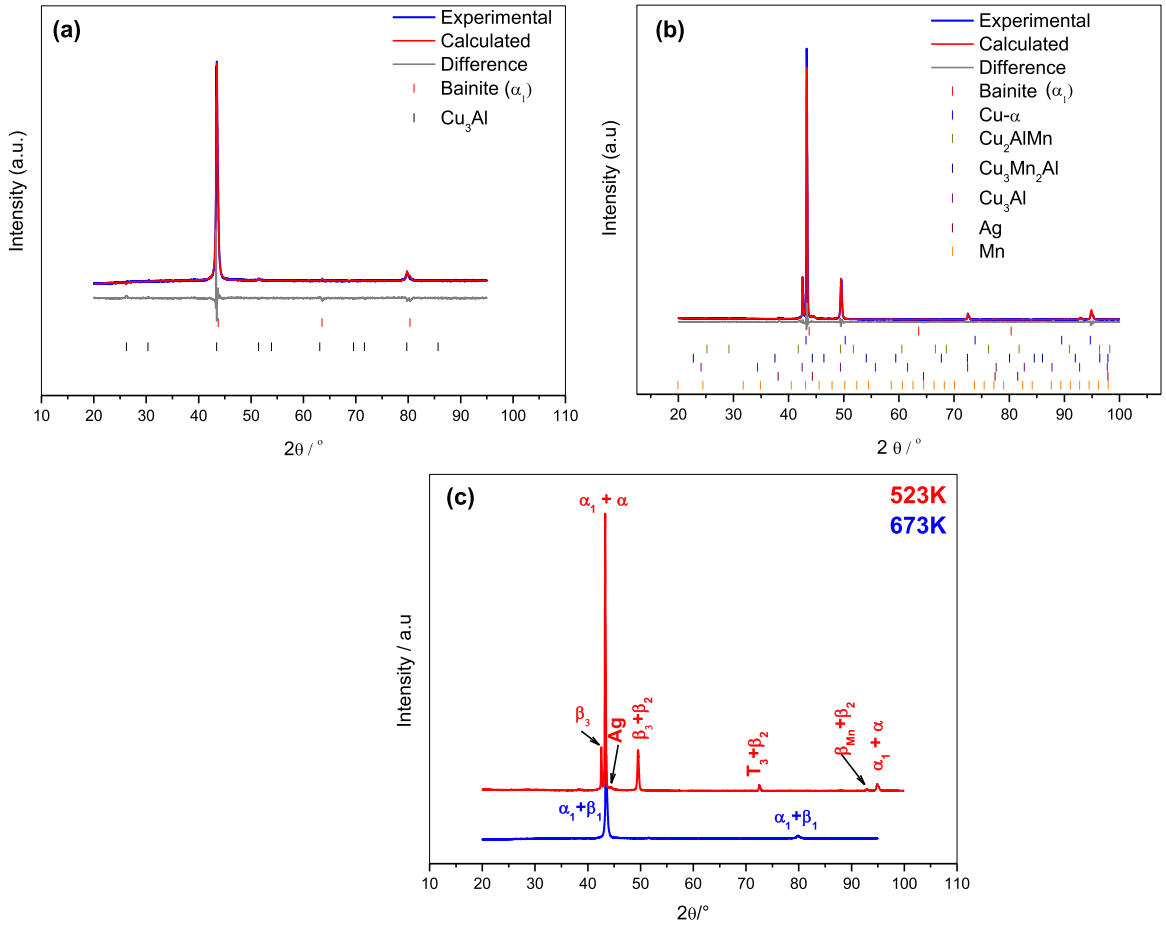

Fig. 6. X-ray diffraction patterns obtained for a sample quenched from 1123 K in iced water and then quenched from 523 K (a) and 673 K (b). (c) Plot for comparison of X-ray diffraction patterns.

Table 1
Parameters obtained from the X-ray diffraction pattern at 523 K using the Rietveld method and the TOPAS software.

Phases	α_1	β_1 ($D0_3$)	Rwp	GOF
Compounds	**Cu**	**Cu_3Al**	3.7	2.3
at%	16.8	83.2		
Space groups	Im3m	Pm3m		

was ascribed to the T_3-Cu_3AlMn_2+α+β_2(B2)→β(A2)+α reaction [4]. The thermal event E_6 can be associated with the decomposition of some residual phase.

In Fig. 3-b one can observe the microhardness with quenching temperature curve obtained as described in $HT_{1\rightarrow2}$ of Fig. 1. This plot shows a hardness decrease between 373 K and 423 K due to the α phase precipitation that occurs before the decomposition of the $\beta_3(L2_1)$ phase. In the temperature range from 523 to 573 K the bainite precipitation and its growth occur, increasing the microhardness values up to 390 HV. It is important to notice that in Cu-Al-Mn alloys the higher microhardness values generally observed are around 350 HV [8].

The formation of the T_3-Cu_3AlMn_2 phase, Ag precipitates, β_{Mn} and α phases together with the lamellae thickening and then bainitic phase decomposition produce a decrease in the microhardness values between 573 and 723 K. After 723 K no significant change was observed on the microhardness values for this alloy composition. In this way, the precipitated silver (in peak E_3) is re-dissolved during heating (in peak E_4), and it shows a very narrow stability range. The presence of Ag also seems to alter the phase stability range and enhances the bainitic precipitation effects on the microhardness values of the Cu-9 wt%Al-10 wt%Mn-3 wt%Ag alloy as compared to literature data [8].

Fig. 4 shows the DSC curves obtained with a heating rate of 10 K min^{-1} for samples of the Cu-9 wt%Al-10 wt%Mn-3 wt%Ag alloy initially submitted to $HT_{1\rightarrow2}$. The quenching temperatures chosen are indicated by arrows in Fig. 3-b and the as-quenched curve was only obtained for comparison (see Fig. 4-a). During this heat treatment the phases expected from heating of the metastable ones at the temperature indicated are produced. On continuous heating, phase transitions that did not occur during heat treatment may be detected, thus allowing the splitting of important thermal events. The heating rate was increased from 3 to 10 K min^{-1} just for optimization of these experiments. In Fig. 4-a one can observe arrows indicating a new thermal event, as compared to Fig. 3-a. This event can be attributed to the α phase precipitation which precedes the decomposition of the $\beta_3(L2_1)$ phase. This decomposition is observed in the DSC curve obtained from the sample quenched from 373 K (peak E_1 in Fig. 4-a). Fig. 4-b shows that in the DSC curves obtained for sample quenched from 523 and 573 K the thermal events E_1 and E_2 are not detected, suggesting that all the bainite phase was already precipitated up to 523 K. This indicates that the microhardness increase shown in Fig. 3-b can be due only to the bainite growth. The arrows in Fig. 4-b indicate endothermic events ascribed to the decomposition of the $\beta_1(D0_3)$ phase and the formation of the T_3-Cu_3AlMn_2, β_{Mn} and α phases. This suggests that there are thermal events overlapping in the same temperature range in which the bainitic precipitation occurs.

In Fig. 4-c the DSC curves obtained for samples quenched from 673, 723 and 773 K show an exothermal thermal event at about 520 K, as indicated by the arrow. This peak is due to the precipitation of Ag retained in the matrix [14,16]. This reaction is only concluded after the formation of the T_3-Cu_3AlMn_2, β_{Mn}, β_2(B2) and α phases since these ones create new diffusion routes with lower Gibbs energy. In the DSC curve obtained for a sample quenched from 773 K it is also possible to see a thermal event at about 770 K that can be due to the T_3-Cu_3AlMn_2 phase decomposition.

Fig. 5 shows the optical micrographs (OM) obtained for samples initially quenched from 1123 K in iced water and then again quenched in iced water from 523, 573 and 673 K. These OM images suggest that the bainitic phase is produced from 523 K and then the growth and thickening of the bainite lamellae occur up to 673 K. This is in accordance with the discussion proposed in Figs. 3-b and 4. Fig. 6 shows the X-ray diffraction patterns obtained for the alloy quenched from 1123 K in iced water and then quenched from 523 K (Fig. 6-a) and 673 K (Fig. 6-b) in iced water. The diffraction patterns in Fig. 6 and Tables 1, 2 also confirm that before the hardness peak, at about 523 K, the $\beta_1(D0_3)$ phase and a small fraction of bainitic phase are dominant, and at about 673 K the T_3-Cu_3AlMn_2, Ag, $\beta_3(L2_1)$, β_2(B2), β_{Mn} and α phases are stable, together with a great fraction of the bainitic phase. These phases were produced from the $\beta_1(D0_3)$ phase decomposition. Fig. 6-c was inserted for better comparison. In Tables 1, 2 the R_{wp} (Weighted profile R-factor) and GOF (Goodness of fit) parameters are indicating the quality of fitting as described in reference [18].

It is known that the presence of the bainitic phase increases the microhardness values [8] and affects the shape memory effect in Cu-based alloys [19,20]. In this work it was possible to verify that the bainitic precipitation is followed by the formation of the T_3-Cu_3AlMn_2, β_{Mn}, β_2(B2) and α phases and then by Ag precipitation. This can disturb the bainite growth and a non-isothermal kinetic analysis of this phase transition could contribute for a better understanding of the reaction mechanism. The analyzed DSC curves (Fig. 7) were obtained at a heating rate slower than that in Fig. 4, thus improving the signal of the thermal event associated with bainitic precipitation. The thermal event E_2 in Fig. 7-a, attributed to the bainite precipitation, is shifted to higher temperatures with the increase of the heating rates, thus suggesting that this reaction is controlled by diffusion. Plots of transformed fraction (y) with absolute temperature were prepared from peak E_2 in Fig. 7-a for the non-isothermal kinetic analysis of this reaction (see Fig. 7-b).

In order to analyze the reaction kinetics, the isoconversional method based on the Model-free kinetics [21,22] was utilized to obtain the activation energy for the bainite precipitation in the Cu-9 wt%Al-10 wt%Mn-3 wt%Ag alloy, considering the peak E_2 in Fig. 7-a and the Eq. (1) [23]:

$$ln\left[\theta_i\left(\frac{dy}{dT}\right)_{y,i}\right]=ln[A_y f(y)]-\frac{E_y}{RT_{y,i}} \quad (1)$$

in which the subscript y designates values related to a given transformed fraction, i is the number of non-isothermal experiments conducted at the heating rates θ_i, $T_{y,i}$ is the absolute temperature, A_y is the Arrhenius constant, E_y is the activation energy and R is the gas constant. By plotting $\ln[\theta_i.(dy/dT)_{y,i}]$ against $1/T_{y,i}$, the value of the E_y for a given y can be obtained. These plots obtained from Eq. (1) were linear with correlation coefficients no less than 0.9892.

Fig. 8 shows the plots of E_y vs. y in which it is possible to observe a conversion dependence of the activation energy in the descending

Table 2
Parameters obtained from the X-ray diffraction pattern at 673 K using the Rietveld method and the TOPAS software.

Phases	α	α_1	β_3 ($L2_1$)	β_2 (B2)	T_3	β_{Mn}	Ag	Rwp	GOF
Compounds	**Cu**	**Cu**	**Cu_2AlMn**	**Cu_3Al**	**Cu_3AlMn_2**	**Mn**	**Ag**	5.8	2.7
at%	0.7	88.9	4.7	0.3	3.1	1.7	0.7		
Space groups	Fm3m	Im3m	Fm3m	Pm3m	Fd-3mS	P4132	Fm3m		

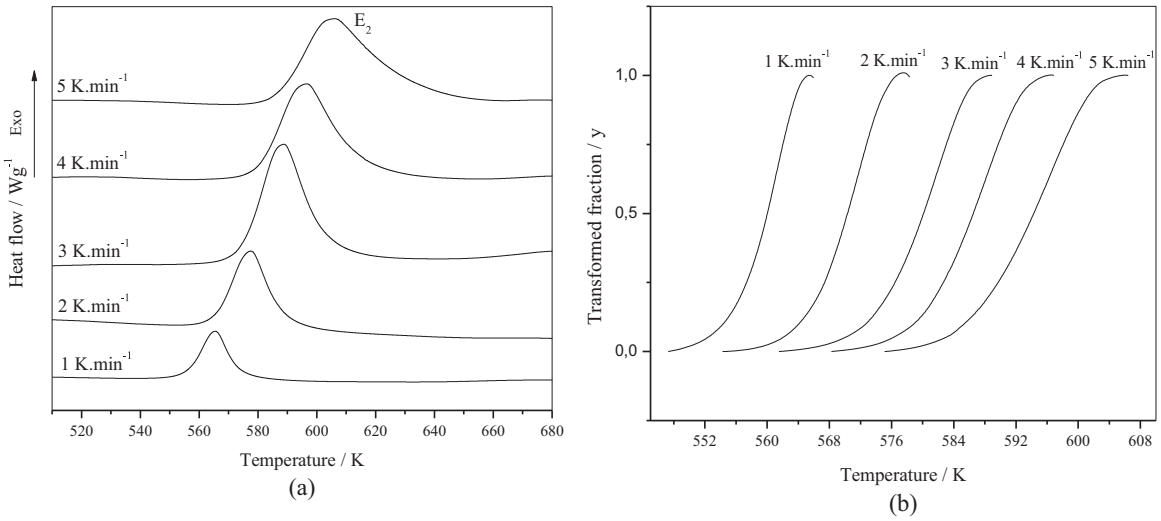

Fig. 7. (a) DSC curves obtained at different heating rates. (b) Plots of transformed fractions vs. temperature.

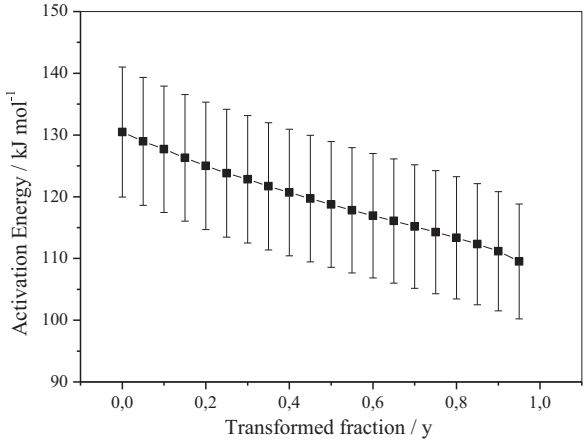

Fig. 8. Activation energy values as a function of the transformed fraction.

shape, suggesting that the reaction mechanism is related to multi-step processes involving a combination between reversible reactions with those complicated by diffusion [22], with an average value of activation energy around 115 kJ mol^{-1}.

The activation energy value found for the bainite precipitation in Cu-Al-Mn alloys is around 60 kJ mol^{-1} [8]. This value was calculated using microhardness measurements, which seem to be more accurate for the bainitic phase precipitation, thus decreasing the interference of other reactions that may occur in low scale.

In this case, the reactions which occur together with the bainitic precipitation contribute significantly for the thermal event E_2 in Figs. 3, 4, and 7-a. The effects of these phase transitions are more pronounced in a non-isothermal method conducted by differential thermal analysis, since the energy of all reactions is measured in the same temperature range. Using microhardness measurements, the activation energy value obtained must be due to the phase that changes the microhardness during the measurements. In Cu-Al-Mn alloys this is ascribed to the bainitic phase [8], what does not decrease the possibility of interference due to perturbation in diffusive processes and precipitates formation. So, differences in activation energy values are also expected in function of reaction monitoring technique.

The higher value obtained in this work may be due to the dissolved Ag in the matrix and to the presence of the T_3-Cu_3AlMn_2, β_{Mn}, β_2(B2), α phases produced in the same temperature range of bainite precipitation and growth. The bainitic phase is richer in Cu than Al and Mn atoms and its growth is suggested to be controlled by diffusion in Cu-Al-Mn alloys [20,24]. There are reports in literature affirming that it has a 9 R structure [19], and recent studies showed a 6 M structure derived from martensite in Cu-Al-Mn alloys [24]. The bainitic phase increases the microhardness [8] and decreases the entropy of Cu-Al-Mn alloys during its formation [25]. Cu-Ag, Cu-Al and Cu-Mn interactions pairs may decrease the Cu diffusion rate and the presence of the T_3-Cu_3AlMn_2, β_{Mn}, β_2(B2), and α phases can also create a physical barrier to the passage of Cu atoms, thus slowing the diffusion and decreasing the Cu fraction available for the bainite formation. These factors can contribute for the slow growth of the bainitic phase, which also promotes an increase in the lamellae thickness and a better accommodation of the phase plates. These effects can increase the microhardness values of the studied alloy in the temperature range in which the bainitic reaction occurs. An additional increase in the bainite lamellae thickness promotes a decrease in the microhardness values, as seen in Fig. 3-b.

4. Conclusions

The results showed that the presence of Ag alters the phase stability range and enhances the bainite precipitation effects on the microhardness values of the Cu-9 wt%Al-10 wt%Mn-3 wt%Ag alloy. The results indicated that the microhardness increase in the studied alloy is only due to the bainite growth step. The results also indicated that the T_3-Cu_3AlMn_2, β_{Mn}, β_2(B2), α phases and Ag precipitates can decrease the Cu diffusion rate in the matrix and increase the average activation energy for the bainite precipitation reaction. It was also possible to verify that the presence of manganese decreases the solubility of silver in the studied alloy and promotes the formation of Ag nanoprecipitates in as-quenched samples. The precipitation of an Ag fraction retained in the matrix during quenching is only concluded after the formation of the T_3-Cu_3AlMn_2, β_{Mn}, β_2(B2) and α phases.

Acknowledgments

The authors thank CNPq and FAPESP for financial support.

References

[1] J.M. Jani, M. Leary, A. Subic, M.A. Gibson, A review of shape memory alloy research, applications and opportunities, Mater. Des. 56 (2014) 1078–1113.
[2] L. Sun, W.M. Huang, Z. Ding, Y. Zhao, C.C. Wang, H. Purnawali, C. Tang, Stimulus-responsive shape memory materials: a review, Mater. Des. 33 (2012) 577–640.
[3] J.X. Xie, J.L. Liu, H.Y. Huang, Structure design of high-performance Cu-based shape memory alloys, Rare Met. 34 (9) (2015) 607–624.
[4] E. Obradó, C. Frontera, L. Mañosa, A. Planes, Order-disorder transitions of Cu-Al-

Mn shape-memory alloys, Phys. Rev. B 58 (21) (1998) 214–255.
[5] Y. Yafet, Ruderman-Kittel-Kasuya-Yosida range function of a one-dimensional free-electron gas, Phys. Rev. B 36 (7) (1987) 3948. http://dx.doi.org/10.1103/PhysRevB.36.3948.
[6] K. Yosida, Magn. Prop. Cu-Mn Alloy. Phys. Rev. 106 (5) (1957) 893. http://dx.doi.org/10.1103/PhysRev.106.893.
[7] R. Kainuma, S. Takahashi, K. Ishida, Thermoelastic martensite and shape memory effect in ductile Cu-AI-Mn alloys, Metall. Mater. Trans. A 27A (1996) 2187–2195.
[8] Y. Sutou, N. Koeda, T. Omori, R. Kainuma, K. Ishida, Effects of ageing on bainitic and thermally induced martensitic transformations in ductile Cu-Al-Mn-based shape memory alloys, Acta Mater. 57 (2009) 5748–5758.
[9] J. Chen, Z. Li, Y.Y. Zhao, A high-working-temperature CuAlMnZr shape memory alloy, J. Alloy. Compd. 480 (2009) 481–484.
[10] R.A.G. Silva, A. Paganotti, S. Gama, A.T. Adorno, T.M. Carvalho, C.M.A. Santos, Investigation of thermal, mechanical and magnetic behaviors of the Cu-11%Al alloy with Ag and Mn additions, Mater. Charact. 75 (2013) 194–199.
[11] S. Yang, F. Zhang, J. Wu, Y. Lu, Z. Shi, C. Wang, X. Liu, Superelasticity and shape memory effect in Cu-Al-Mn-V shape memory alloys, Mater. Des. 115 (2017) 17–25.
[12] D. Balzar, N.C. Popa, Analyzing microstructure by Rietveld refinement, Rigaku J. 22 (1) (2005) 16–25.
[13] A.A. Coelho, J. Evans, I. Evans, A. Kern, S. Parsons, The TOPAS symbolic computation system, Powder Diffr. 26 (S1) (2011) 22–25.
[14] A.T. Adorno, M.R. Guerreiro, R.A.G. Silva, Kinetics of Ag-rich precipitates formation in Cu-Al-Ag alloys, Mater. Sci. Eng. A 374 (2004) 170–176.
[15] Y. Sutou, T. Omori, A. Furukawa, Y. Takahashi, R. Kainuma, K. Yamauchi, S. Yamashita, K. Ishida, Development of medical guide wire of Cu-Al-Mn–base superelastic alloy with functionally graded characteristics, Mater. Res. Part B Appl. Biomater. 69B (2004) 64–69.
[16] A.T. Adorno, M.R. Guerreiro, C.A. Ribeiro, C.T.R. Guerreiro, Influence of silver additions on the thermal behavior of the Cu-8wt%Al alloy, J. Therm. Anal. Cal. 64 (2001) 1141–1146.
[17] R.A.G. Silva, A. Paganotti, A.T. Adorno, C.M.A. Santos, T.M. Carvalho, Characteristics of the Cu-18.84at%Al-10.28at%Mn-1.57at%Ag alloy after slow cooling from high temperatures, J. Therm. Anal. Cal. 121 (2015) 1233–1238.
[18] Brian H. Toby, *R* factors in Rietveld analysis: how good is good enough?, Powder Diffr. 21 (1) (2006) 67–70.
[19] V. Asanovic, K. Delijic, N. Jaukovic, A study of transformations of β-phase in Cu-Zn-Al shape memory alloys, Scrip. Mater. 58 (2008) 599–601.
[20] J. Dutkiewicz, E. Cesari, Phase transitions during continuous heating of martensitic CuAlMn alloys, J. De. Phys. IV Coll. 05 (C2) (1995) (C2-199-C2-204).
[21] A.T. Adorno, T.M. Carvalho, A.G. Magdalena, C.M.A. dos Santos, R.A.G. Silva, Activation energy for the reverse eutectoid reaction in hypo-eutectoid Cu-Al alloys, Thermochim. Acta 531 (2012) 35–41.
[22] S. Vyazovkin, C.A. Wight, Kinetics in solids, Annu. Rev. Phys. Chem. 48 (1998) 25–49.
[23] S. Vyazovkin, A.K. Burnham, J.M. Criado, L.A. Pérez-Marqueda, C. Popescu, N. Sbirrazzuoli, ICTAC kinetics committee recommendations for performing kinetic computations on thermal analyses data, Thermochim. Acta 520 (2011) 1–19.
[24] S. Motomura, T. Hara, T. Omori, R. Kainuma, M. Nishida, Morphological and chemical analysis of bainite in Cu-17Al-11Al (at%) alloys by using orthogonal FIB-SEM and double-EDS STEM, Microscopy (2016) 1–10. http://dx.doi.org/10.1093/jmicro/dfw003.
[25] Y. Sutou, N. Koeda, T. Omori, R. Kainuma, K. Ishida, Effects of aging on stress-induced martensitic transformation in ductile Cu-Al-Mn-based shape memory alloys, Acta Mater. 57 (2009) 5759–5770.